Evolution of radial and energy distributions in two-photon double ionization of He in near-femtosecond fields

Adam Prior,[1] Henri Bachau,[2,*] and L. A. A. Nikolopoulos[1,†]
[1]*School of Physical Sciences, Dublin City University, D09 V209 Dublin, Ireland*
[2]*Centre des Lasers Intenses et Applications, Centre National de la Recherche Scientifique, CEA, Université de Bordeaux, 33405 Talence Cedex, France*

(Received 21 March 2023; revised 4 July 2023; accepted 7 September 2023; published 17 October 2023)

In this paper we study the emergence of two-electron wave packets following the two-photon ionization of helium with intense near-femtosecond pulses. Monitoring the dynamics of the doubly ionized portion of the joint radial and energy distributions during the pulse's lifetime, we observe and examine the effects of strong Coulombic interactions which take place between electrons with partial waves other than the dominant *pp* channels. The generated doubly ionized wave packets correspond to configurations where the two electrons remain close to the core and roughly equidistant until the pulse's peak; it is at later times that the sequential or nonsequential nature of the double-ionization process leads to distinctly different patterns. Moreover, we also show the difference in the evolution into the corresponding final-state distributions as the pulse's central photon energy varies between 42 and 70 eV and, thus, as the ionization mechanism transforms from the so-called nonsequential to the sequential ionization regime, respectively.

DOI: 10.1103/PhysRevA.108.043110

I. INTRODUCTION

Double photoionization (DI) is of special importance in atomic and molecular physics, as it provides insights into the dynamics of strongly correlated quantum systems and may provide the means to clarify the often competitive role between the external electromagnetic field and the interelectronic interactions, taking place during the ionization process. For example, interelectronic interactions may radically affect the observed radial, kinetic-energy, and angular patterns of the ejected electrons. Given the complexity of such ionization processes, their theoretical description is invaluable to understanding and interpreting experimental reports, especially in view of the current status in the generation of intense subfemtosecond soft-x-ray sources provided by free-electron lasers (FELs) and high-harmonic radiation [1–6].

DI may proceed either via a single-photon absorption, linear to the field's intensity interaction process, observed even in the weak-field regime (e.g., synchrotron radiation) [7], or as a highly nonlinear process by multiphoton absorption using intense long wavelength radiation [8,9]. Both single and multiphoton DI have been investigated extensively in the past decades, each one contributing its merit to the understanding of the role of the electronic correlations in the double-photoionization process. In the case of single-photon DI the theoretical treatments, often ignoring the temporal nature of the field, employ either traditional perturbation theory [7,10,11] or methods which reformulate the relevant time-dependent Schrödinger equation (TDSE) into a set of coupled states as for example is done in the converged close-coupling method in [12] and in [13] where the nonperturbative Floquet method was applied. On the other hand, since in multiphoton DI the interaction with the field is highly nonlinear the direct solution of TDSE is vital in order to develop a realistic theory [14,15]. In between these two cases the two-photon double ionization (TPDI) of rare gases presents some interesting properties which facilitate its experimental and theoretical study; TPDI requires sufficiently intense pulses with photon energies in the UV or soft-x-ray regime. Such pulses have recently become available not only with FELs but also with Ti:sapphire high-harmonic generation sources [16]. In response to the availability of these radiation sources, within the past 30 years a vast number of theoretical works have studied the TPDI of noble gases with pulses of few femtoseconds in duration [17–33], relying on nonperturbative approaches, like the resolution of the TDSE or time-dependent perturbation theory. As a result, to date, a quite sufficient understanding of the TPDI mechanisms (discussed in more detail in the next paragraph) has been achieved and experimental data are currently interpreted on this basis [34–39]. Very briefly, for the case of DI with few femtosecond pulses a clear distinction between sequential double-ionization (SDI) and nonsequential double-ionization (NSDI) mechanisms is possible and the theoretical calculations from the various groups are convergent in their predictions for the ionization yields, final energies, angular distributions, and cross sections [24,25,28,29,31–33,40].

The TPDI of atomic helium represents a special case as it is free from complications originating from the presence of further electrons in the core region; it requires laser fields with central photon energies of at least 39.5 eV, since

*Permanent address: BP 119, 49 cours Pasteur, 33000 Bordeaux, France.
†Corresponding author: lampros.nikolopoulos@dcu.ie

 ©2023 American Physical Society

helium's double-ionization threshold is ≈79 eV. Therefore, in principle, the absorption of two photons with $\omega > 39.5$ eV may lead to He^{2+} and two liberated electrons; for such fields the ejection times of the electrons will be relatively close and for this reason this ionization mechanism is known as *nonsequential* (or direct) double ionization. However, an essential qualitative and quantitative change occurs when the photon energy becomes higher than the ionization threshold of singly ionized helium (He^+), which is ≈54.4 eV. In this case, double ionization proceeds initially by the absorption of one photon from the neutral helium, which may lead to the formation of He^+ followed by the absorption of one further photon by the He^+ ion which also results in doubly ionized helium, He^{2+}, and two free electrons; as this double-ionization process first requires relaxation to any of the He^+ bound states, and as this takes some time, it is generally known as *sequential* DI. Due to this timewise sequential nature of photon absorptions, SDI requires minimal electron-electron (*e*-*e*) interactions. It goes without saying that this assumption gains in validity for longer pulses rather than shorter pulses (in the limit of pulses with duration shorter than the relaxation time to He^+ the condition of sequential ionization becomes pointless). Therefore, we may assume two photon energy regions—the first one between 39.5 and 54.4 eV, where NSDI is the exclusive mechanism for double photoionization, and the second energy regime with $\omega > 54.4$ eV, where, in principle, both NSDI and SDI are responsible for double photoionization.

Following the conclusions of many theoretical and experimental studies for pulses with durations of a few femtoseconds (and more), the ionization mechanisms and the final kinetic and angular distribution are very distinctive between these two ionization mechanisms [17,18,31,32,40]. For example, if energetically available, SDI is much more probable than NSDI for the same photon energy regardless of the field's intensity. Furthermore, the singly differential kinetic-energy distribution for SDI is dominated by two peaks separated by the difference of the ionization potentials of neutral and singly ionized helium, $\Delta I = 54.4 - 24.6 = 29.8$ eV. In contrast, in the case of NSDI, the same distribution lacks such peaks [41]. These observations are quite well documented for few femtosecond pulses and one can easily infer some conclusions about the ionization dynamics from the available spectra.

In contrast to this wealth of works in the regime for multifemtosecond pulses, the TPDI with pulses of duration shorter than or on the order of femtoseconds has not yet been studied in the same detail, possibly due to the lack of sufficiently intense subfemtosecond duration pulses. For TPDI with such pulses the fact that the characteristic interelectronic correlation time is of similar order (>140 as) [40] makes the distinction between SDI and NSDI mechanisms less clear and the correspondence between experimental spectra and dynamics begins to fade. The same complication in the distinction between SDI and NSDI occurs when the pulse's central photon energy is close to the He^+ ionization threshold (54.4 eV), as, due to the pulse's frequency bandwidth, both ionization mechanisms contribute to the overall double ionization. Another aspect of the TPDI which is also not well explored is its dynamics during the pulse as most of the studies were focused on postpulse DI results. From an experimental viewpoint the situation now has changed in view of recent technological advances which allow for soft-x-ray pulses of near-femtosecond or subfemtosecond (1 fs) duration with intensities sufficiently high to induce two-photon ionization of most rare gases, including helium [16,42–44]. The availability of short duration pulses allows for the possibility of pump-probe ionization schemes which can be utilized to trace the ionization dynamics temporally; in other words, not only are the final ionization products routinely experimentally available, but nowadays there is the possibility to investigate in detail how the ionized system progresses in time towards its final states. As such, the temporal evolution of doubly excited states represents an interesting case of study, being a typical case of a strongly correlated dynamical system [45–48]; therefore, along similar thinking the temporal evolution of the TPDI represents another such possibility.

With these observations in mind, in the present paper we study the dynamics of TPDI for subfemtosecond pulses with central photon energies spanning the regime of SDI and NSDI. In particular, we study the two-electron joint radial and kinetic-energy distributions following two-photon double ionization for a number of photon energies, from the viewpoint of a partial-wave analyzed two-electron wave packet. As it is not straightforward to identify the individual roles played by the laser field and the interelectronic interactions in the overall double-ionization process, we attempt to do this based on the calculated time evolution of radial and energy distributions when the pulse is still active. The rapid evolution of these distributions over the pulse cycles brings new physical insight into the dynamics of double ionization from the transient regime to the identified mechanisms of direct and sequential double ionization at the end of the pulse. Moreover, and in contrast to most published results, we have calculated and plotted only the portion of the double-ionization patterns which consist purely of unbound orbitals (both orbitals of positive energy); this is possible due to the particular spectral basis approach used which allows us to isolate the part of the wave function corresponding to two-electron excitations, even for photon energies where the SDI channels dominate. It is worth pointing out here that such disentanglement between singly and doubly excited configurations is not trivial, if not impossible at all, using either a grid [15,26,31] or a nonspectral basis [30,40] representation of the two-electron wave function.

In Sec. II we present the main equations leading to the calculation of the two-electron radial and energy spectra. Since the formulation has been developed and discussed elsewhere as well, we present only the formulas for the quantities of special interest to the present paper.

In Sec. III we discuss the contribution of the individual partial-wave channels to the double-ionization process, the dynamics of the generated two-electron wave packets, and their energy patterns in the presence of the pulse; in the same section, we also present the final radial and energy distributions as the pulse's photon energy varies between 42 and 70 eV, an energy range marking the transition from the direct to the sequential regime.

In Sec. IV we present the conclusions of our paper. For the equations presented in this paper, Hartree units are used.

II. THEORETICAL FORMULATION

In the following, the formulation for the *ab initio* calculation of the two-electron joint radial probability distribution is presented. Briefly, we calculate the two-electron wave function, evaluated until the end of the laser pulse, and then extract the desired information either by evaluating the squared modulus of the two-electron wave function or by projecting the wave function onto zeroth-order functions.

The method of calculating the electronic structure of helium (CI two-electron states expanded on a B-splines basis), and its dynamics under the interaction with a laser field, is discussed in detail in [49,50] and in a different context in [51,52]; here we discuss the details of the theoretical formulation that are necessary for our particular purposes. We should also note that the calculation of the present method was compared with calculations originating from a similar method developed and tested over the years for helium. More specifically we have compared the helium energies, dipole matrix elements, and continuum spectrum density with those obtained from a non-spectral basis method where the two-electron wave function is expanded directly on a B-spline basis as developed in [27]. Reviews on the use of the B-spline basis in theoretical atomic and molecular physics can be found in [53,54].

A. *Ab initio* calculation of helium atomic structure

We initially construct the two-electron singlet antisymmetric uncorrelated basis with well-defined angular momentum values, L, as the solutions to the eigenvalue problem of the zeroth-order Hamiltonian, $\hat{H}_0 = \hat{h}_1 + \hat{h}_2$, where the one-electron He^+ Hamiltonian is given by

$$\hat{h}_i(\mathbf{r}_i) = -\frac{1}{2}\nabla_i^2 - \frac{2}{r_i}, \tag{1}$$

where i indexes the two electrons. Following a rather standard angular momentum coupling algebra, these solutions, in a spherical coordinate system, with its origin placed at the helium nucleus, may be expressed as

$$\phi_{ab}^L(\boldsymbol{r}_1, \boldsymbol{r}_2) = A_{ab}\frac{P_a(r_1)}{r_1}\frac{P_b(r_2)}{r_2}\mathcal{Y}_{l_1 l_2}^{L0}(\Omega_1, \Omega_2), \tag{2}$$

where $a \equiv (n_1 l_1)$, $b \equiv (n_2 l_2)$, and $\mathcal{Y}_{l_1 l_2}^{L0}(\Omega_1, \Omega_2)$ are the $M_L = 0$ bipolar spherical harmonics, containing the angular momentum coupling coefficients (Clebsch-Gordon coefficients). To ensure that the states are of singlet symmetry the angular quantum numbers are subject to $l_1 + l_2 + L = 0, 2, 4, \ldots$ and $A_{ab} = (1 + a \leftrightarrow b)/\sqrt{2(1 + \delta_{ab})}$, with the $a \leftrightarrow b$ interpreted as an exchange of the state indices a and b.

The radial orbitals $P_{nl}(r)$ are determined as the solutions of the radial eigenvalue equation for the He^+ Hamiltonian, namely,

$$\left[-\frac{1}{2}\frac{d^2}{dr^2} + \frac{l(l+1)}{2r^2} - \frac{2}{r}\right]P_{nl} = \epsilon_{nl}P_{nl}(r). \tag{3}$$

The purely radial functions, $P_{nl}(r)$, are numerically solved by expanding the radial functions on a piecewise polynomial basis (B-spline basis). The choice of this particular basis is dictated by its numerical ability for representing continuum states, a property which is of importance in the particular case where ionized atomic states are involved [49,54,55]. The He^+ system is assumed to be confined in a sphere of radius R, much larger than typical atomic sizes ($R \gg 1$ a.u.). Within our particular approach we implement the so-called fixed boundary conditions, which require the wave functions to strictly vanish at the origin and the boundaries, $P_{nl}(R) = 0$. As a result of this requirement the He^+ eigenstates of Eq. (1) are discretized, allowing the bound and continuum spectrum to be represented by negative- and positive-energy orbitals, respectively, subject to the unity normalization. Therefore, the index n of $P_{nl}(r)$ takes integer values, $n = 1, 2, \ldots$, and the sign of ϵ_{nl} determines the nature of the radial orbital: exponentially decaying (negative) or oscillatory (positive).

Having completed the numerical calculation of the partial-wave radial orbitals of He^+, the helium Hamiltonian is modeled by

$$\hat{H} = \hat{H}_0 + \frac{1}{|\mathbf{r}_1 - \mathbf{r}_2|}, \tag{4}$$

with the second term on the right-hand-side representing the interelectronic interaction potential. The eigenvalue problem to be solved is the time-independent Schrödinger equation:

$$\hat{H}\Phi_{EL}(\boldsymbol{r}_1, \boldsymbol{r}_2) = E_L\Phi_{EL}(\boldsymbol{r}_1, \boldsymbol{r}_2), \tag{5}$$

where $\Phi_{EL}(\boldsymbol{r}_1, \boldsymbol{r}_2)$ represents the two-electron eigenstates of $\hat{H}$. Following the interaction of helium with a linearly polarized laser, only the $M_L = 0$, singlet symmetry states $(S, M_S) = (0,0)$ are excited since the total magnetic quantum number and the initial spin state do not change.

For the solution of Eq. (5), a configuration-interaction (CI) method is employed where the helium eigenstates, Φ_{EL}, are expanded on the zeroth-order two-electron basis $\phi_{ab}^L(\boldsymbol{r}_1, \boldsymbol{r}_2)$:

$$\Phi_{NL}(\boldsymbol{r}_1, \boldsymbol{r}_2) = \sum_{ab} c_{ab}^{NL}\phi_{ab}^L(\boldsymbol{r}_1, \boldsymbol{r}_2). \tag{6}$$

Since the expansion is on discretized orbitals, the resulting two-electron CI states are also discretized, along with their associated energy, E. For this reason it is more consistent to use a discretized notation for the states and the energy, thus using $E_L \to E_{NL}$ and $\Phi_{EL} \to \Phi_{NL}$, $N = 1, 2, \ldots$.

Substituting Eq. (6) into Eq. (5), followed by projection over $\phi_{ab}^L(\boldsymbol{r}_1, \boldsymbol{r}_2)$, converts it to a matrix equation which, upon diagonalization, retrieves the eigenenergies, E_{NL}, and the CI amplitude coefficients, c_{ab}^{NL}. In the helium case, there are two characteristic energies, related with the ground-state energy of neutral (E_0) and singly ionized (E_1) helium, measured relative to the DI threshold energy, which here is, conventionally, set to zero (and $E_2 = 0$ eV); the experimental values of these are $E_0 \approx -79.03$ eV and $E_1 \approx -54.42$ eV (for comparison our calculated values were -78.88 and -54.42 eV). Within the approximations introduced in the numerical computation of the discretized states, it turns out that a two-electron eigenstate with $E_{NL} < E_1$ is of bound character and thus represents helium bound states, while states with energies $E_1 < E_{NL} < 0$ represent singly ionized helium states with an ejected electron. Finally, the numerical states with $E_{NL} > 0$ may represent both singly and doubly ionized helium with one electron ejected or two electrons ejected, respectively.

B. TDSE of helium in a laser field

Once the electronic structure of the helium atom has been solved for, its dynamics is calculated via the TDSE for the helium-laser system:

$$\imath\frac{\partial}{\partial t}\Psi(\mathbf{r}_1,\mathbf{r}_2,t)=[\hat{H}+\hat{D}(t)]\Psi(\mathbf{r}_1,\mathbf{r}_2,t), \tag{7}$$

where Ψ is the time-dependent wave function and $\hat{D}(t)$ describes the external laser interaction dipole potential in the Coulomb gauge:

$$D(t)=\frac{1}{c}A(t)\hat{z}\cdot(\hat{\boldsymbol{p}}_1+\hat{\boldsymbol{p}}_2), \tag{8}$$

where $\hat{z}$ is the unit vector along the z axis and $\boldsymbol{p}_1$ and $\boldsymbol{p}_2$ are the electron momenta. $A(t)$ is the amplitude of the electromagnetic potential field related to the electric field of the pulse by $E(t)=-\dot{A}(t)/c$. Note that the long-wavelength approximation has been taken into account in the expressions above.

In this paper we choose for the amplitude

$$A(t)=A_0\sin^2\left(\frac{\pi t}{\tau_p}\right)\sin\,\omega t,\quad 0\leqslant t\leqslant\tau_p, \tag{9}$$

where ω is the carrier frequency. The use of a squared sinusoidal envelope satisfies the requirements that the envelope varies slowly with respect to the carrier period, and rises and falls to zero; τ_p is the laser pulse duration, related to the field period ($T_0=2\pi/\omega$) by $\tau_p=n_cT_0$, where n_c is the number of field cycles in the pulse. The associated frequency full width at half maximum (FWHM) bandwidth of this pulse is given by $\Delta\omega=1.44\,\omega/n_c$ [40].

A spectral expansion of the solution of Eq. (7) in terms of the two-electron CI eigenstates with time-dependent amplitude as

$$\Psi(\boldsymbol{r}_1,\boldsymbol{r}_2,t)=\sum_{NL}C_{NL}(t)\Phi_{NL}(\boldsymbol{r}_1,\boldsymbol{r}_2) \tag{10}$$

allows the interpretation of $|C_{NL}(t)|^2$ as the population of the state Φ_{NL} since it represents the probability of observing the system in state $\Phi_{NL}(\mathbf{r}_1,\mathbf{r}_2)$ at time t.

Formally, upon substitution of this latter expansion into Eq. (7) and multiplying from the left by $\Phi^*_{N'L'}(\boldsymbol{r}_1,\boldsymbol{r}_2)$, followed by spatial integration over the entire coordinate space, the TDSE transforms into a set of coupled ordinary differential equations:

$$\imath\dot{C}_{NL}(t)=E_{NL}C_{NL}(t)+\sum_{N'L'}D_{NL;N'L'}(t)C_{N'L'}(t), \tag{11}$$

where $D_{NL;N'L'}$ are the dipole matrix elements between the CI states Φ_{NL} and $\Phi_{N'L'}$. Standard angular momentum algebra allows for the expression of the two-electron dipole matrix elements in terms of the $c^{NL}_{n_1l_1n_2l_2}$ CI coefficients and the one-electron dipole matrix elements; the latter are calculated numerically given the $P_{nl}(r)$ radial functions [49]. Thus solving the TDSE amounts to calculating only the two-electron dipole matrix elements and integrating Eq. (11) to find the time-dependent coefficients, $C_{NL}(t)$.

C. Radial and kinetic-energy distributions

At this point we are in the position to proceed with the main subject of the present paper, the electron's radial and kinetic-energy distributions, to express the two-electron distributions in terms of the CI coefficients c^{NL}_{ab} of Eq. (6) and time-dependent coefficients $C_{NL}(t)$ Eq. (10).

Projection of the zeroth-order two-electron wave function, (2), on the time-dependent wave function, $\Psi(\boldsymbol{r}_1,\boldsymbol{r}_2,t)$, followed by the full spatial integration, results in the joint photoelectron energy distribution (J-PED):

$$P(e_1,e_2,t)=\sum_{Ll_1l_2}P_{l_1l_2}(e_1,e_2) \tag{12}$$

where $P_{l_1l_2}(e_1,e_2)=\sum_L|\sum_N c^{NL}_{n_1l_1;n_2l_2}C_{NL}(t)|^2$ is the partial J-PED and $(e_1,e_2)=(\epsilon_{n_1l_1},\epsilon_{n_2l_2})$ are the kinetic energies associated with the $P_{n_1l_1}(r)$ and $P_{n_2l_2}(r)$ radial orbitals, respectively. The calculation of the J-PED for energy points other than the (e_1,e_2) points is based on standard interpolation methods.

The two-electron joint photoelectron radial distribution (J-PRD) results in the angular integration of the square of the time-dependent wave functions, $\int d\Omega_1 d\Omega_2|\Psi(\boldsymbol{r}_1,\boldsymbol{r}_2,t)|^2$, leading to

$$P_r(r_1,r_2,t)=\sum_{l_1l_2}P_{l_1,l_2}(r_1,r_2,t), \tag{13}$$

where $P_{l_1,l_2}(r_1,r_2,t)=\sum_L|\chi^{(L)}_{l_1l_2}(r_1,r_2,t)|^2$ is the partial J-PRD and

$$\chi^{(L)}_{l_1l_2}(r_1,r_2,t)=\sum_{Nn_1n_2}C_{NL}(t)c^{(NL)}_{n_1l_1;n_2l_2}\rho_{n_1l_1;n_2l_2}(r_1,r_2), \tag{14}$$

with

$$\rho_{n_1l_1;n_2l_2}(r_1,r_2)\equiv\frac{P_{n_1l_1}(r_1)P_{n_2l_2}(r_2)+P_{n_2l_2}(r_1)P_{n_1l_1}(r_2)}{\sqrt{2\left(1+\delta_{n_1l_1;n_2l_2}\right)}}.$$

This distribution represents the probability distribution of finding the two electrons with angular momenta (l_1,l_2) at radial distances r_1 and r_2 from the helium's center of mass. Note that, under the given conditions, the radial distribution is symmetrical to the exchange $r_1\leftrightarrow r_2$, meaning that $P_r(r_1,r_2,t)=P_r(r_2,r_1,t)$ for orbitals $(n_1l_1)\leftrightarrow(n_2l_2)$. Accordingly, the J-PRD and J-PED are diagonally symmetric.

III. RESULTS AND DISCUSSION

For the calculations we have used laser pulses with central carrier frequency $\omega=42$–70 eV, at an intensity $I_0=10^{14}$ W/cm^2. As the number of cycles is kept constant ($n_c=12$), the pulse durations range between 0.71 and 1.17 fs, with bandwidths from 5 to 8.5 eV, dependent on the carrier frequency (see Table I). The bandwidths, $\Delta\omega$, in this table are calculated as the FWHM of $|\tilde{A}(\omega)|^2$ where $\tilde{A}(\omega)$ is defined as the Fourier transform of the field $\tilde{A}(\omega)=\int_0^{\tau_p}dtA(t)e^{-\imath\omega t}$; we find for these that $\Delta\omega\simeq1.44\times2\pi/\tau_p$ (in a.u.). An analytical expression for the $\tilde{A}(\omega)$ can be found in [56].The helium electronic structure is calculated by using the singlet-symmetry two-electron wave-function expansion in Eq. (6) with $L,l_1,l_2\leqslant3$. We have checked that, for the 12 cycles

TABLE I. The pulse duration for the used pulses. In all cases the number of field cycles n_c is 12.

ω (eV)	42	45	**48**	**50**	**52**	**54**	**56**	**58**	63	**70**
τ_p (fs)	1.17	1.10	1.03	0.99	0.95	0.92	0.89	0.86	0.78	0.71
$\Delta\omega$ (eV)	5.05	5.4	5.76	6.0	6.24	6.48	6.72	6.96	7.56	8.4

used for pulses, our results do not change in any significant way by increasing L, l_1, l_2, or the box radius $R = 60$ a.u. ($\approx$3.2 nm).

In all plots the most significant contribution comes from the $(l_1, l_2) = (1, 1) = pp$ wave, then the $(0, 2) = sd$ one, followed by the $(0, 0) = ss$ and $(2, 2) = dd$ partial waves. The doubly ionized channels may have either $L = 0$ or 2 total angular momentum as a result of the two-photon absorptions from the $L = 0$ helium ground state.

A. NSDI and SDI final-state distributions

For the discussion of the NSDI and SDI mechanisms we first take specific photon energies; first, in Fig. 1 we show the calculated two-electron J-PED (upper plot) following TPDI by a $\omega = 42$ eV pulse. The extended spread of the J-PED around the line $e_1 + e_2 \sim E_0 + 2\omega = 0.184$ a.u. (5 eV) is characteristic, a feature which is common for pulses with central photons well below the DI threshold of 54.4 eV. In the same figure, the two-electron J-PRD final pattern (bottom plot) is concentrated along the diagonal $r_1 = r_2$ as the result of this evenly shared energy among the two electrons; therefore, the distances of the ejected electrons from the He^{2+} residual ion are relatively the same, even if they are ejected along different directions. It is worth noticing that these results are in agreement with previous works [27,40,57] where it was shown that, for photon energies well below 50 eV, the electrons tend to share the same energy, while close to threshold the electron energy distribution is more U shaped (also in agreement with the results presented below). In these works it was also demonstrated that, well below the SDI threshold, the electrons are preferentially ejected with back-to-back configuration with $r_1 = r_2$, resulting from strong angular correlations. More specifically, at ultrashort time scale, the absorption of one photon by each of the electrons produces the dominant pair of angular momenta (1,1), while at longer times it is entangled with the (0,2) channel (other angular pairs are also entangled but to a lesser extent), producing the configuration of back-to-back electron ejections [27]. Under these conditions the radial correlations play an essential role since shortly after their ejection the electrons experience different effective charges (i.e., dynamical screening) and it is only at later times they acquire roughly the same energy and are located at similar distance from the nuclei. At these times the effective charge of the nucleus is the same for both electrons and the screening becomes static [27]. We are turning now to the case of TPDI in the presence of a 70-eV photon energy pulse. In Fig. 2 we show the two-electron J-PED (top plot) and J-PRD (bottom plot) for the pp partial-wave channel (which in our calculation shows up as the dominant one). In sharp contrast to the 42-pulse case, the majority of the electrons are ejected with kinetic energies peaked at $e_1 = E_0 + \omega_1 - E_1 \approx 1.67$ a.u. (45.4 eV) and $e_2 = E_1 + \omega_2 - E_2 \approx 0.57$ a.u. (15.6 eV) and with unequal radial distances as the joint distributions generally peak at $r_1 \neq r_2$.

A qualitative discussion based on these results can follow at this point. The value of the He^+ ionization potential ($I_1 = E_2 - E_1 = 54.4$ eV) determines the photon energy regimes for two distinct TPDI mechanisms to occur. A pulse with average photon energy above 39.5 eV, following the absorption of two photons of energy ω_1 and ω_2 with $E_0 + \omega_1 + \omega_2 > 0$, suffices to create doubly ionized helium ions (ω_1 and ω_2 may differ but are restricted to lie within the bandwidth of any

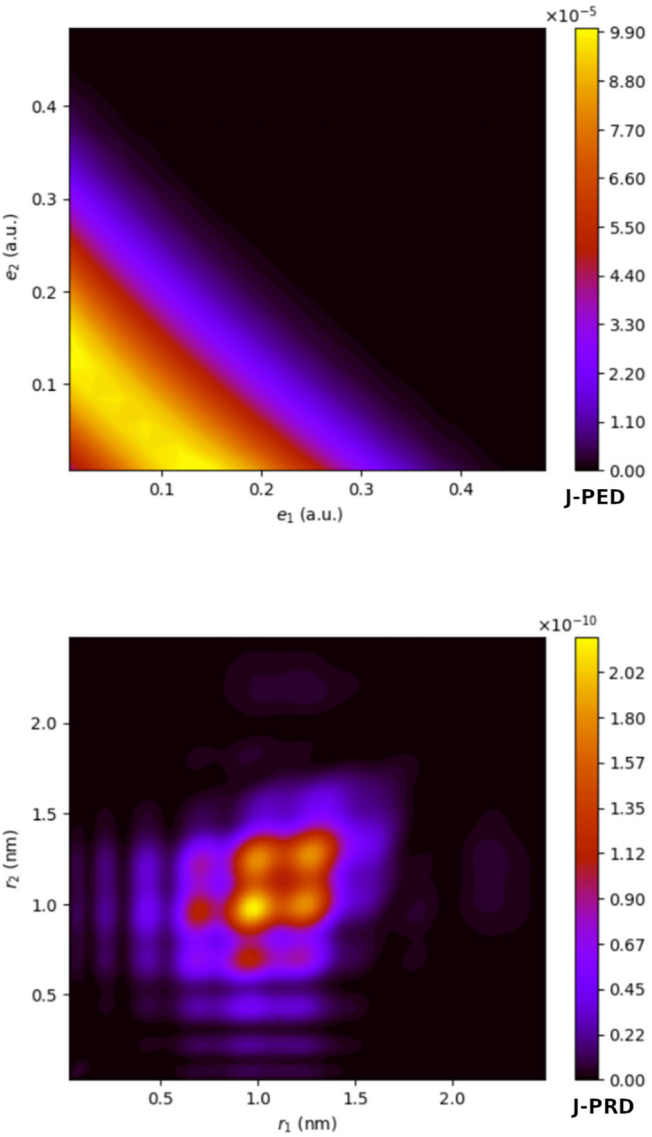

FIG. 1. The J-PED (top plot) and J-PRD (bottom plot) expansions are plotted for a pulse with 1.17-fs $\omega = 42$ eV average photon energy of 10^{14} W/cm^2 intensity at the end of the pulse (cycle 12).

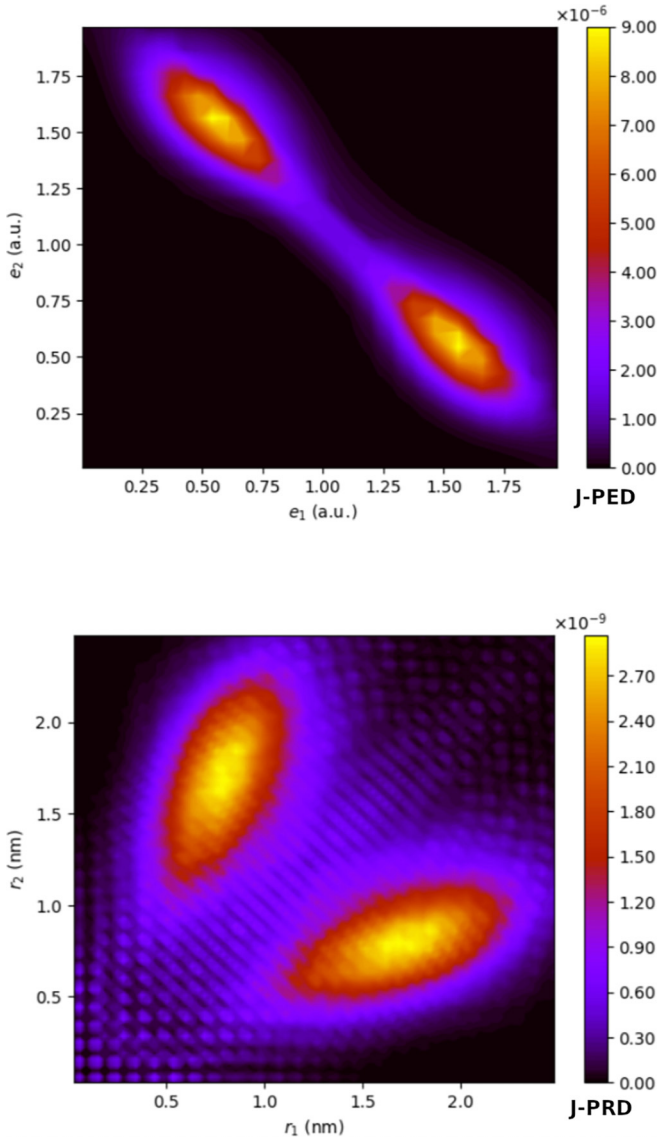

FIG. 2. Plots of the partial J-PED (top) and J-PRD (bottom) $(l_1, l_2) = (1, 1)$ channel, following interaction with a 0.71-fs $\omega = 70$ eV pulse of 10^{14} W/cm^2 intensity. The projection time is the end of the pulse (cycle 12).

given pulse). Therefore, energywise, and within the framework of a CI representation, the absorption of two photons generates a two-electron wave packet which may include channels with two positive-energy one-electron He^+ orbitals $e_1 > 0, e_2 > 0$, and thus both of unbound nature; however, timewise, depending on the time elapsed between the two-photon absorptions the generated two-electron wave packets may be associated with radically different final kinetic-energy and radial patterns. A portion of the wave packet, corresponding to photon absorption events close in time, consists of orbitals which all have quite equal probability to excite, provided they satisfy the energy requirement $e_1 + e_2 = E_0 + \omega_1 + \omega_2$. The spatiotemporal probability for this portion of the wave packet to show up depends mostly on the corresponding angular momentum values $(l_1, l_2; L)$, via the amplitude $\chi^{(L)}_{l_1 l_2}$ given in Eq. (14).

The same energy condition may be satisfied by ionization channels with one of the orbitals being of bound nature $(e_1 < 0, e_2 > 0$ and vice versa); this part of the two-electron wave packet represents singly ionized helium final states and is not of our concern in the current investigation.

An alternative ionization mechanism results when the two-photon absorptions occur at times which differ by an amount which is larger than the relaxation time τ_r of He^+ which is of the order of $\tau_r \approx 2\pi/|V_c| \approx 140$ as, where $V_c = E_0 - (2E_1 - E_2) = I_1 - I_0 = 1.095$ a.u. (see [40] and other references therein). In this case, the primary wave packet, generated by the first-photon absorption, evolves to a state $\psi_t^+ \sim \phi_{nl}\phi_{e_1}$, resembling a $He^+(nl)$ bound orbital and an outgoing wave packet with central energy peaked at $e_1 = E_0 + \omega_1 - E_{nl}$ where E_{nl} is the energy of $He^+(nl)$. The subsequent time evolution of this two-electron wave packet depends on whether the absorption of the second photon (with energy ω_2) suffices to promote the bound electron to a continuum state. For example, ignoring for clarity indistinguishability issues and suppressing the time variable, if the residual ion has relaxed to the $He^+(1s)$ state, so that $\psi_t^+ \sim \phi_{1s}(r_2)\phi_{e_1}(r_1)$, then if $\omega_2 < 54.4$ eV the absorption of one more photon cannot lead to a transition of $He^+(1s) \rightarrow He^+(\epsilon p)$ (it may proceed though via above threshold ionization by further exciting the continuum wave packet $\phi_{e_1}(r_1)$ and leading to $\psi_t^+ \sim \phi_{1s}(r_2)\phi_{e_1+\omega_2}(r_1)$, eventually corresponding to singly ionized helium and therefore not of our interest here). On the other hand, if $\omega_2 > 54.4$ eV, it is much more probable for the transition $He^+(1s) \rightarrow He^+(\epsilon p)$ to occur [rather than $\phi_{e_1}(r_2) \rightarrow \phi_{e_1+\omega_2}(r_2)$], leading to a wave packet of the type $\psi_t^{2+} \sim \phi_{e_2 p}(r_2)\phi_{e_1 p}(r_1)$ with $e_2 \sim E_1 + \omega_2 - E_2$; this latter mechanism represents the so-called sequential DI as opposed to nonsequential (or direct) DI, described earlier.

Therefore, the sequential mechanism is rather energy and timewise constrained as it necessitates pulses with photon energies $\omega > 54.4$ eV and durations longer than the relaxation time of the residual He ion to He^+ (140 as). It leads to a kinetic-energy spectrum peaked at e_1 and e_2 which for moderate intensities have a width mainly determined by the pulse's bandwidth. From the dipole selection rules, in the final state, the wave packets have $l = 1$ angular momenta and therefore are (p, p) channels, characterized by the radial probability distribution $|\chi_{11;L}|^2$, $L = 0, 2$. It is important to bear in mind that, in the SDI regime, we also may have "simultaneous" photon absorptions but it is expected that their contribution to the two-electron wave packet is not the dominant one.

In Fig. 2 the uneven kinetic-energy sharing, also leading to an uneven radial distance, is indeed reproduced by the calculations. We may make some rough estimates about the expected radial peak positions. Since the kinetic-energy peaks are located around the 1.67- and 0.57-a.u. energies, we take as average speeds for the outgoing wave packets $v_1 = \sqrt{2 \times 1.67} = 1.83$ a.u. and $v_2 = \sqrt{2 \times 0.57} = 1.07$ a.u. (group velocities in a more technical parlance), correspondingly. It is most probable that the wave packets will be born at times just before the peak of the pulse, so we take this "birth" time to be the peak of the fifth cycle (out of 12 cycles). It is also well established that the first ejected electron acquires most of the correlation energy and as such it

corresponds to the peak with the largest kinetic energy. Therefore, since the pulse's total duration is 0.71 fs, the journey time may be estimated to be about $t_1 \approx (7/12)\tau_p = 0.414$ fs (17.13 a.u.), thus giving a radial distance of about $R_1 \sim v_1 t_1 = 1.83 \times 17.13 = 31.33$ a.u. (1.66 nm). Following the same reasoning we also find $R_2 \sim v_2 t_2 = 1.07 \times 11.4 = 12.5$ a.u. (0.66 nm); since the second photon absorption occurs after the residual ion has relaxed to He^+ the traveling time for the second electron is at least 140 as (5.8 a.u.) shorter than t_1, thus we take $t_2 \sim t_1 - 5.8 = 11.4$ a.u. Comparing this with the *pp* radial distribution, we can see that the peaks are indeed approximately these distances. Continuining with the 70-eV pulse, in Fig. 3, we show the radial distributions for the next three strongest doubly ionized partial channels included in the two-electron wave packet; generally they consist of orbitals with kinetic energies satisfying $e_1 + e_2 = E_0 + 2\omega > 0$, which means e_1 and e_2 may take values of $[0, 61]$ eV and resemble NSDI processes as the electrons emerge closer in radial distance; this is especially true for the *sd* channel (middle plot in Fig. 3). These channels are weaker though (relative to the dominant *pp* channel) as their angular momenta require electron-electron interactions to take place in addition to the interaction with the external laser field. The laser is the primary excitation agent during double ionization, but the wave packets also evolve in the presence of the residual ion $(-2/r)$ and the interelectronic $\approx 1/|\mathbf{r}_1 - \mathbf{r}_2|$ *static* potentials. Since these terms are taken into account in the field-free Hamiltonian, they do not contribute to changes of the total energy and angular momentum of the combined system $He^{2+} + e^- + e^-$, but affect the two-electron wave-packet composition among the various partial channels; in other words, in addition to the electric dipole transitions which may change the total energy $E = e_1 + e_2$ and $L = l_1 + l_2$, transitions between $(e_1 l_1; e_2 l_2) \rightarrow (e_1' l_1'; e_2' l_2')$ are allowed as long as $e_1 + e_2 = e_1' + e_2'$ for a given L. The strength of these static potentials drops with the distance from the core region and the interelectronic distance, so it is reasonable to expect that the partial waves resulting from such interactions represent parts of the doubly ionized wave packet with the two electrons on average spatially close to each other. It should also be pointed out that some of these channels will also be *pp* partial waves but their contribution will be overwhelmed by the sequentially generated *pp* wave packets.

Based on this discussion, the plots in Fig. 3 show weaker partial channels compared to the *pp* channel associated with the SDI mechanism; also, their radial distributions are generally broader around the $r_1 = r_2$ diagonal. The fact that they are generally closer radially ($r_1 \sim r_2$) indicates that they are generated within a shorter time interval because their primary excitation is energetically relatively evenly distributed, thus acquiring comparable energies; this shorter time interval leads to energetically (and spatially) broader distributions than the sequential *pp* channel. Therefore, features characteristic of interelectronic interactions are still present though not dominating. So, these contributions to the wave packets are mainly produced by absorption of two photons relatively close in time, near the peak of the pulse. For such wave packets, the traveling time is between t_1 and t_2 and this explains why the center of the radial wave packet is located between the R_1 and the R_2 estimated earlier.

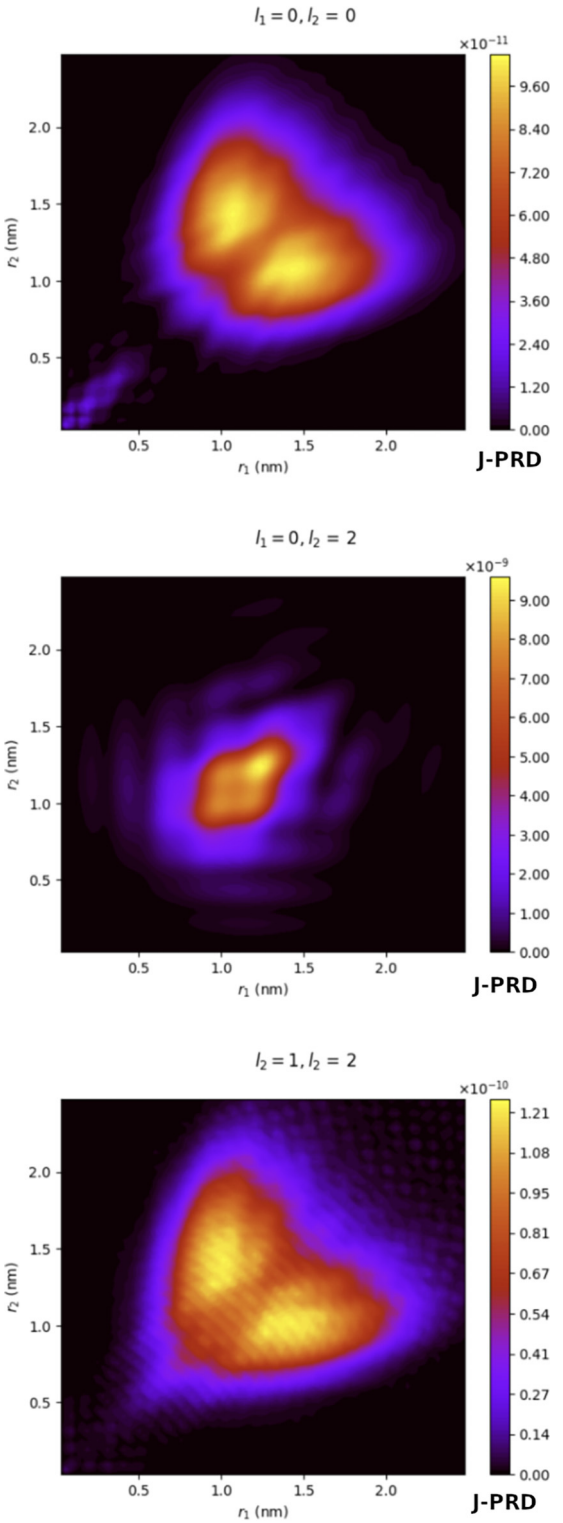

FIG. 3. Plots of the partial J-PRD, for the next three stronger channels, following the *pp* channel shown in the bottom plot of Fig. 2. These are the *ss*, *sd*, and *dd* channels. Projection time is the end of the pulse (cycle 12).

We now turn our attention to the case of the NSDI process and in Fig. 4 we present the first four dominant partial J-PRDs for the case of the 45-eV pulse. First, in all cases, we notice that the doubly ionized wave packets are well concentrated

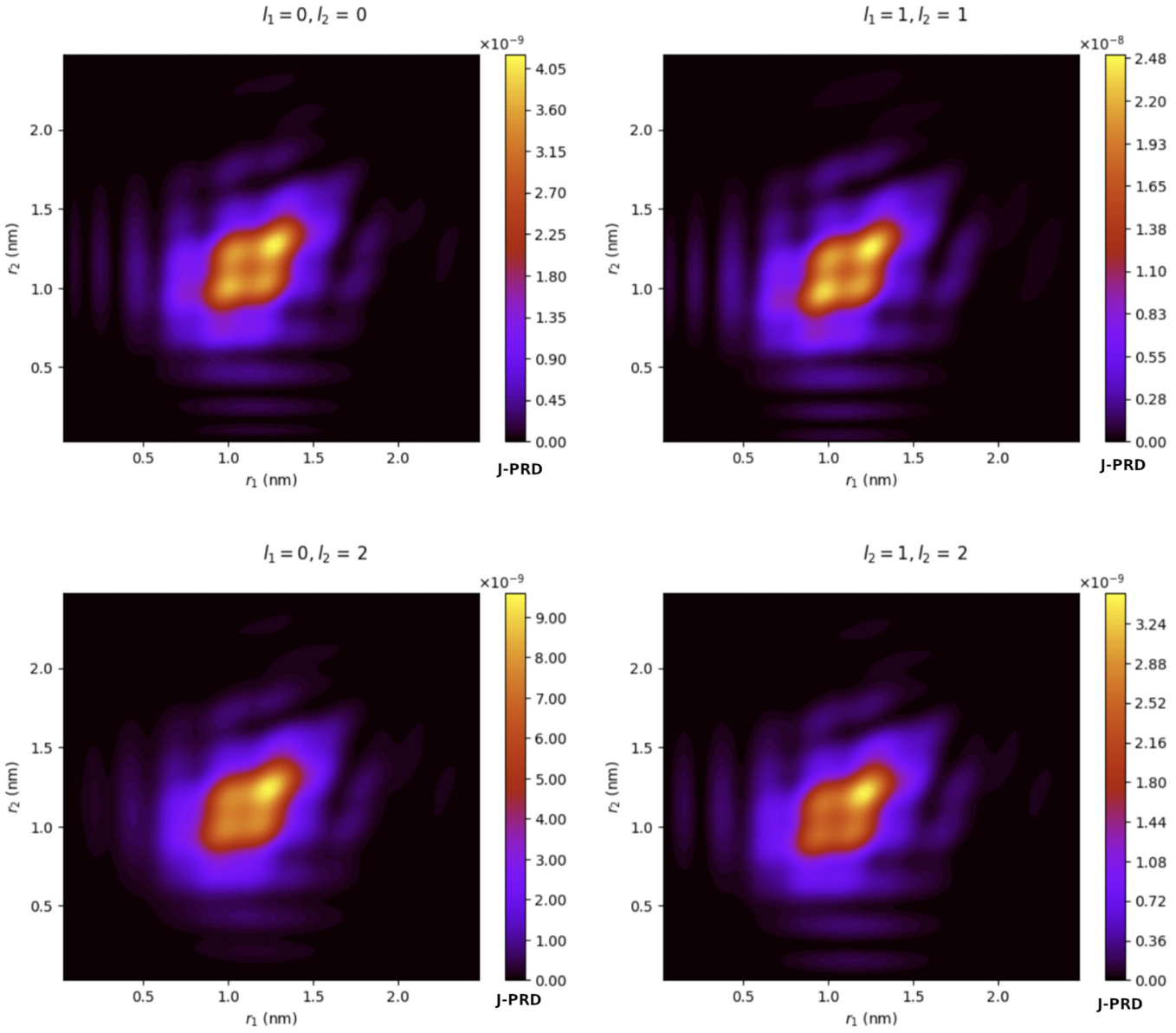

FIG. 4. The first four dominant channels of the partial J-PRD are plotted in the NSDI regime for a 12-cycle (1.1-fs) 45-eV average photon energy pulse of 10^{14} W/cm^2 peak intensity. Projection time is the end of the pulse (cycle 12).

around the $r_1 = r_2$ diagonal. Again, the pp channel gives the larger contribution to the total wave packet, similar to what is observed in the SDI regime. The ss, sd, and dd channels, which require e-e interactions, have a very different radial pattern than the corresponding ss, sd, and dd channels for the 70-eV pulse in Fig. 3; clearly in the latter case the patterns are a mixture of sequentially and nonsequentially ejected electronic wave packets.

So, for $\omega < 54.4$ eV pulses, the dominant ionization mechanism is the NSDI channel while, for the $\omega > 54.4$ eV pulses, SDI is dominant. The main difference is that for the former, while the primary interaction is the radiation field, the electron-electron interaction may contribute significantly in the overall double-ionization process, whereas for the SDI case the contributions of the electron-electron interaction are greatly diminished in the pp channel; this reduction is not as severe in the other channels, though. In the SDI, and for the dominant pp channel, interelectronic interactions are not a prerequisite to fulfill angular momentum rules and they do not affect those portions of the two-electron wave packet which correspond to energetically and spatially distinct configurations for the two emerged electrons; nevertheless a minimal contribution of the latter is always present. In other words, in the case of the pp channel the angular momentum and energy conservation rules are automatically fulfilled by the rules obeyed from the electric dipole transitions alone. Following this thinking the order of significance of the sd, ss, and dd channels may be attributed to the particulars of the electron-electron correlation interactions for transitions other than those leading to a pp channel.

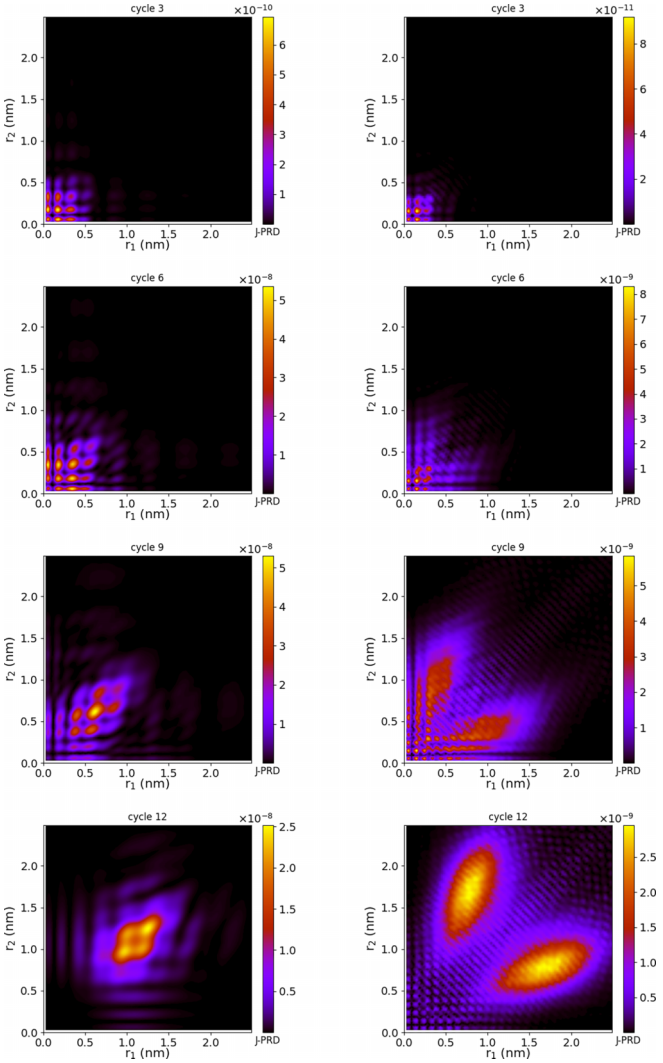

FIG. 5. Time evolution of the (1,1) partial-wave 2-e J-PRD ($E, e_1, e_2 > 0$) in the NSDI (left column, $\omega = 45$ eV) and the SDI (right column, $\omega = 70$ eV) regimes. Remaining pulse parameters as in Figs. 2 and 4. r_1 and r_2 are given in nm $= 10^{-9}$ m.

B. Variation with time

We now examine the quantitative differences of the temporal radial probability patterns during the NSDI and the SDI processes. In the plots of Fig. 5 we provide snapshots of the radial distribution of the wave packets for a 45-eV (left plot) and 70-eV (right plot) pulse. For these plots we have used Eq. (13) with the summations in Eq. (14) restricted to $N, n_1,$ and n_2 such that $E > 0, e_1, e_2 > 0$. These plots show the different time evolutions of the NSDI and SDI double-ejection processes.

Since the calculations were performed in the velocity gauge, we have chosen the snapshots corresponding to times where the field vanishes and the interpretation of the time-dependent coefficients as field-free probability amplitudes for the He eigenstates is temporarily restored; this way we have the means to calculate the time evolution of the radial distributions during the pulse's lifetime. In both cases, the generated two-electron wave packets build up initially in the proximity of the core at distances of no more than 0.5 nm and around the $r_1 = r_2$ diagonal for up to the pulse's maximum (sixth cycle). The J-PRDs reveal a nonuniform production of the continuum wave packets with a bunched sequence following the oscillating field. The SDI and NSDI J-PRDs start to develop differently around the fourth cycle where it becomes evident that the NSDI distribution remains concentrated around the $r_1 = r_2$ diagonal. We should bear in mind the time taken for the residual ion (following one-photon absorption) to relax to He^+, which is about 140 as, corresponding to about $140/59.2 \approx 2.4$ cycles for the 70-eV pulse (the pulse period is 59.2 as).

Concentrating for the moment on the SDI J-PRD in Fig. 5, the formation of the asymmetric radial distribution is due to the enhancement of double-ejection channels originating from a further photon absorption later in time; the latter seems to dominate the pattern after the eighth cycle and leads to a peaked oval shape. In other words, two excitation mechanisms are observed in these plots; first a small portion of the wave packet gets excited, consisting of channels with both electrons in the continuum, traveling along the $r_1 = r_2$ diagonal; the remaining (larger) portion corresponds to channels with only one electron ejected (not shown in the plots) but soon after (past the pulse's peak) its presence overwhelms the distribution since the bound electron in the He^+ is also ejected, following the absorption of the second photon.

On the other hand, in the NSDI J-PRD for the 45-eV pulse, as seen in the left plot of Fig. 5, the sequential ionization mechanism is absent at later times, thus the electronic wave packet continues to remain concentrated along the $r_1 = r_2$ diagonal, throughout the field's lifetime. In this case the distribution's final formation takes place after the field has passed its peak and stopped generating new DI wave packets. During and after the eighth cycle the wave packets appear to depart from the core region and merge with each other, eventually leading to a smoother wave packet traveling along the diagonal line. At these later times, apart from the natural broadening of free-moving wave packets, electron-electron interactions are taking place which cause the redistribution of population between the partial waves $\chi_{l_1,l_2}(r_1, r_2)$.

These observations are also present in the corresponding J-PED patterns, shown in Figs. 6 and 7 for the 70- and 45-eV pulses, respectively. We can see that the J-PED patterns initially are evenly distributed among the partial waves of the DI wave packets for both the 45- and 70-eV cases; in the SDI case though (the 70-eV pulse), considering that the vast amount of ionization will occur around the fourth or fifth peak of the pulse and that it takes 2.5 cycles for the He to relax to He^+, one reasonably expects any appreciable asymmetric energy distribution to show up after the sixth or seventh oscillation peak of the field, which is what we see in the plots for the 70-eV pulse. Eventually, inspection of the final plot (cycle 12) of Fig. 6, again for the 70-eV pulse, shows consistency with the observation that the SDI is overwhelmed by channels where one of the electrons is ejected from He, with energy $e_1 = E_0 + \omega - E_1 \approx 45$ eV (1.67 a.u.), and the other from He^+ with energy $e_2 = E_1 + \omega - E_2 \approx 15.6$ eV (0.57 a.u.). In contrast, for NSDI, for the 45-eV pulse, an evenly distributed final pattern is observed, due to the absence of further ionization of He^+ ions. It is worth noting though

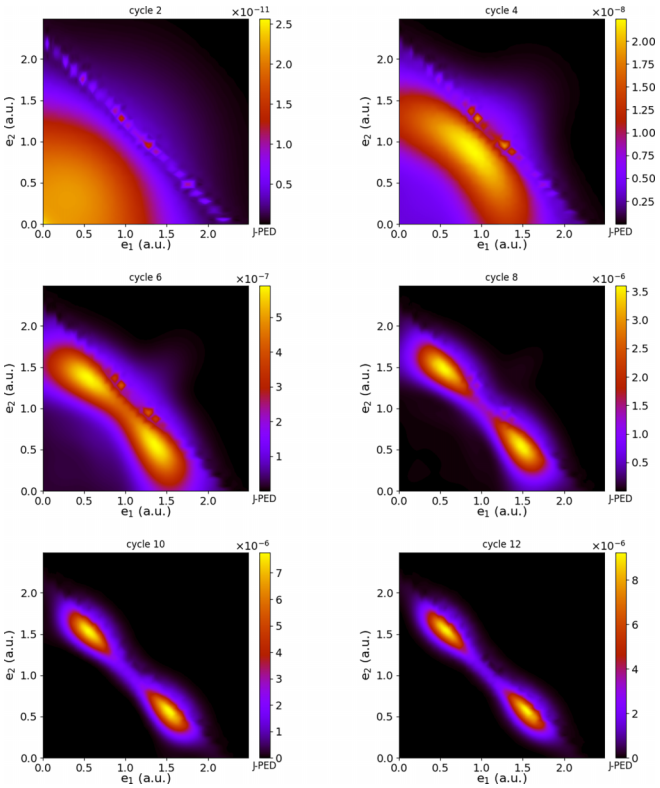

FIG. 6. The time evolution of the (1,1) partial-wave J-PED for the 70-eV pulse with parameters as in Fig. 2. e_1 and e_2 are given in atomic units (a.u.).

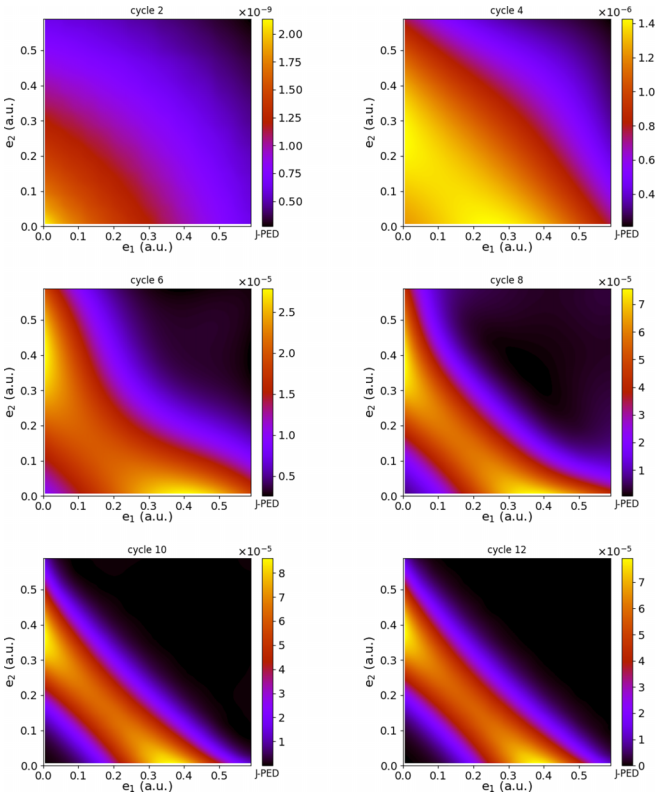

FIG. 7. The time evolution of the (1,1) partial-wave J-PED for the 45-eV pulse with parameters as in Fig. 4. e_1 and e_2 are given in atomic units (a.u.).

that for the dominant pp channel, in the NSDI regime, the two electrons may get ejected with comparable energies but with their momenta pointing in the same or opposite directions (back-to-back ejection); in the latter case the two electrons evolve practically independently of each other as their inter-electronic interactions are minimized, while in the former case dynamical screening effects take over between the various partial-wave channels [40].

In Figs. 2 and 4 we observe the characteristic features of the 70- and 45-eV pulse to be a double-peak versus single-peak radial pattern, respectively. It is interesting to examine how these patterns vary with the pulse's photon energy as the latter crosses the DI 54.4-eV threshold.

C. Variation with the photon energy

We have calculated the final distributions for a number of such cases and the results are plotted in Fig. 8. At first glance we notice that the final distributions do not clearly belong to the NSDI case (represented from the 42- and 45-eV pulses) and the SDI case (represented by the 70-eV pulse). The J-PRDs for the 45- and 70-eV pulses are shown in the top left and bottom right plots, respectively; the other seven plots correspond to interaction with 48-, 50-, 52-, 54-, 56-, 58-, and 63-eV 12-cycle pulses at $I_0 = 10^{14}$ W/cm^2. In these plots we observe the gradual deformation of a single-peak pattern along the diagonal line to a multipeak asymmetric pattern as the photon energy crosses the 54.4-eV DI threshold, finally leading to the twin-peak structure for the highest photon 70 eV. It is also worth noting that the multipeak structures are aligned with the r_1 and r_2 axes, which suggests that the double ejection occurs with one of the electrons moving outwards while the other moves very slowly. This is possibly not surprising as the second electron is excited from broadband pulses with photon energies around 54.4 eV. For example the 12-cycle 56-eV pulse has a bandwidth of ≈7 eV as seen from Table I, so the final distribution pattern has contributions from ionization paths via both the direct ($\omega < 54.4$ eV) and the sequential ($\omega > 54.4$ eV) DI mechanism. For photon energies close to the threshold ($\omega \approx 54.4$ eV) we notice a sliced structure, very different from the ones obtained in the regime of NSDI ($\omega = 45$ eV) or SDI ($\omega = 70$ eV). We recall that, due to the laser bandwidth, the nonsequential or sequential character of double ejection is not clearly defined in this region. We consider the case of $\omega = 54$ eV; focusing on the left part of the graph, we observe vertical slides ranging from $r_2 \approx 1.0$ nm to $r_2 \approx 2.5$ nm and from $r_1 \approx 0$ nm to $r_1 \approx 1.2$ nm, suggesting the ejection of a rapid electron (e_2) and a slower one (e_1). The sliced structure of the J-PRD implies that this pattern may be attributed to the field's variation, with bursts of ejected electrons at the field maxima. Indeed, once the first electron is ejected the second one can be ejected at the same time or during the following maxima of the field, resulting in the sliced structure observed. In order to strengthen this assertion we calculate the single-electron radial distribution, obtained by integration along one of the radial coordinates:

$$P(r_1, \tau_p) = \int_0^R dr_2 \, P_r(r_1, r_2, \tau_p). \tag{15}$$

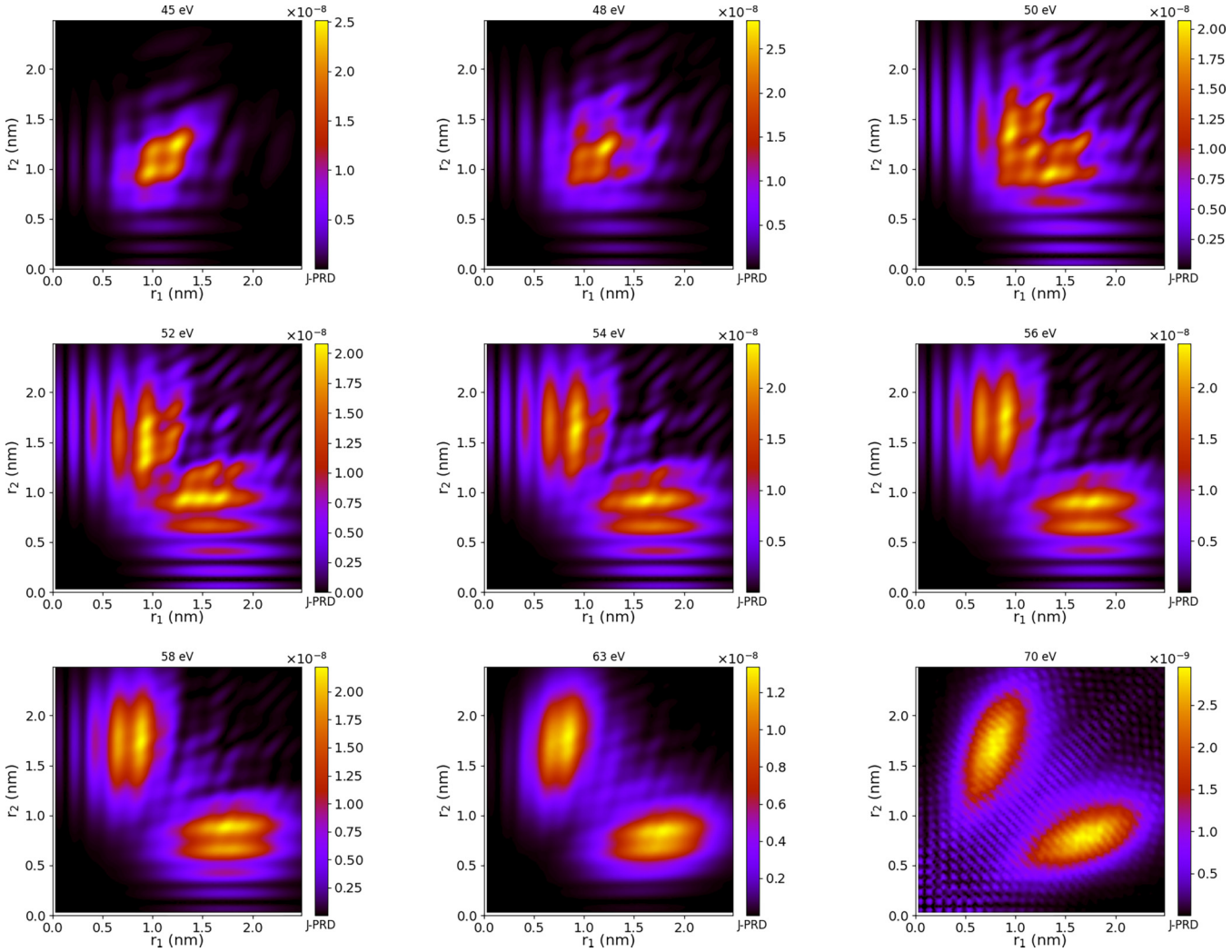

FIG. 8. Clearly visible in the (1,1) partial-wave J-PRD patterns is the transition from the direct to the sequential double-ionization regime as the photon energy varies from 45 to 70 eV for a 12-cycle pulse. Projection time is the end of the pulse (cycle 12). The pattern transitions from a singly peaked distribution where the electrons are likely to be the same distance from the core, to a doubly peaked distribution where one of the electrons is likely to be further from the core than the other as a consequence of the sequential nature of the ionization process. r_1 and r_2 are given in nm $= 10^{-9}$ m.

Of course, due to the symmetry of the distribution, integration over the other radial coordinate results in identical values, so that $P(r_1, \tau_p) = P(r_2, \tau_p)$. The results of the calculations are shown in Fig. 9. As suggested above, the various peaks in this spectrum may be attributed to the field's variation, which peaks twice within an oscillation period, representing bursts of ejected electrons; in this intermediate DI regime it is not straightforward to make quantitative estimations which would attribute this sliced pattern to a field-cycle induced ejection assertion just based on the pulse's properties (photon energy, duration) and the helium's electronic structure. This plot can be understood as follows: at the initial stages of ionization the distribution over kinetic energies is very broad (see cycles 2–6 of Fig. 7), corresponding to the farthest parts of the 1-e radial distribution $P(r_1, \tau_p)$, which also shows a large broad structure for all photon energies. At the later stages of the ionization, the energy distribution develops an asymmetry which resembles a SDI process (see cycles 8–12 of Fig. 7), where one of the electrons takes most of the kinetic energy while the other is left behind with a much smaller kinetic energy. For these later ionization times (after the pulse's peak) we observe a striking similarity with the corresponding plots of radial distributions observed from ionization of single-electron systems (i.e., hydrogen); the wave packet shows well-separated peaks in accordance with the field's oscillation period [58]. It is not straightforward to estimate the distance traveled from an outgoing two-electron wave packet with nonzero angular momenta and in close proximity with a dynamically screened core and in the presence of a laser field [59]; such an investigation requires a more elaborate and quantitative examination, including consideration of the joint angular distribution, which will provide us information about the wave packet's ejection direction. Nevertheless, we may make a rough estimation by taking the case of $\omega = 56$ eV; in this case the wave number for this "fast" electron is $k_{56} = \sqrt{2 \times 1.15} \simeq 1.52$ a.u. In one period of the field $T_{56} \simeq 3.07$ a.u. each "burst" of the wave packet travels a distance $r \simeq k_{56} \times T_{56} = 4.6$ a.u. $= 0.243$ nm, which is approximately the

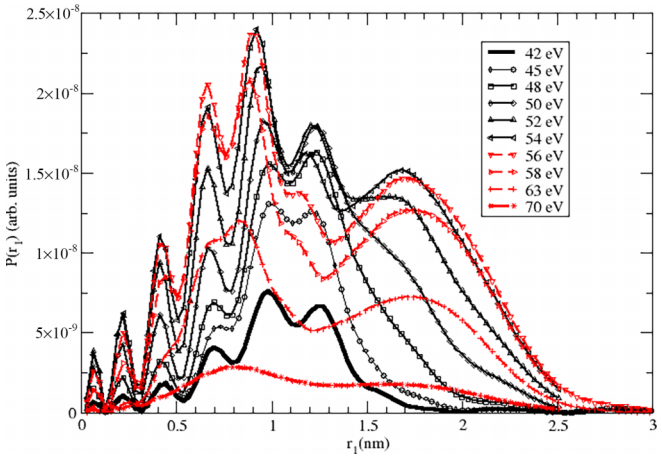

FIG. 9. The results of integration of the (1,1) partial J-PRD over one radial coordinate are shown for pulses of $\omega = 42$–70 eV. Projection time is the end of the pulse (cycle 12). The peaks in the radial distributions are associated with the laser cycle period. The units in the vertical axis are arbitrary for each of the photon energies for visibility reasons.

distance between the two highest peaks in Fig. 9 for the $\omega = 56$ eV. The fact that the peak's radial separation matches the field's period indicates a back-to-back ejection of the two electrons in accordance with theoretical predictions [24,31,32]. Possibly, the safest estimation to associate the peaks in the radial distribution with the field's oscillation is to use the field's bandwidth as a measure of the wave-number spread in the wave packet; for example, in the case of the 56-eV pulse we have a bandwidth of $\Delta\omega = 0.23$ a.u.; we associate this with the bandwidth of the kinetic energies in the ejected wave packet and set $\Delta\epsilon_{56} = 0.247$. But since $\Delta\epsilon_{56} = k_{56}\Delta k_{56}$ we then have $\Delta k_{56} = \Delta\epsilon_{56}/k_{56} = 0.247/1.52 \simeq 0.163$ a.u. Now, if we repeat the same calculation for, say, $\omega = 52$ eV, we find $\Delta k_{52} = \Delta\epsilon_{52}/k_{52} = 0.23/1.342 \simeq 0.171$ a.u.; this shows that the first peak in the $P(r_1, \tau_p)$ radial distribution for 52 eV (yellow line) should be broader than the one corresponding for 56 eV (red line), and this is what we see in the plot.

Next, in Fig. 10 we show the variation of the energy distributions with the energy; the first observation is the gradual transition of the J-PEDs from a relatively flat and symmetric pattern to a peaked asymmetrical pattern. Clearly the peaks in the spectra eventually tend to satisfy

$$e_1 \simeq E_0 + \omega - E_1, \quad e_2 \simeq E_1 + \omega - E_2, \tag{16}$$

where one of the electrons is likely to obtain more energy than the other as a consequence of the sequential nature of the ionization process. In the same figure one may observe the similarity between the patterns in the SDI regime (e.g., 63 eV) with those in the NSDI regime (e.g., 52 eV). The difference is that in the SDI case e_1 and e_2 have positive values (corresponding to continuum orbitals) while in the NSDI regime only a portion of the peaks is realized with both orbitals of positive energy and in accordance with Eq. (16); the remaining portion looks like that it has leaked outside the $(e_1 > 0, e_2 > 0)$ plane, towards energetically high Rydberg states. Note that a special feature of our plots is that only orbitals where both $e_1 \geqslant 0$ and $e_2 \geqslant 0$ are included. The plots corresponding to the NSDI regime suggest that, had we included orbitals with either $e_1 < 0$ or $e_2 < 0$, the energy distributions would also tend to peak to orbitals with (negative) energies according to Eq. (16), corresponding to high-energy Rydberg states, but this is exactly what we call SDI and conceptually would not differ from the NSDI apart from the fact that it proceeds via the Rydberg states (quasicontinuum). Unfortunately, due to the small box size, the discrete basis states with negative energy near the zero-energy threshold do not correspond to physical high-energy Rydberg states and we had to restrict the configuration space of the plotted distributions. A related work, using a semiquantitative approach, can be found in [60].

IV. CONCLUSIONS

By directly solving the time-dependent full-dimensional two-electron Schrödinger equation for helium in the field of a laser pulse, we investigate the time evolution of the emerged radial wave packets during the two-photon double ionization via both the nonsequential and the sequential mechanisms.

We have carried out a systematic analysis of the joint radial and energy distributions of the two-electron wave packet and elucidated some aspects of the role of electron correlations in the presence of the pulse. In all cases the dominant ionization channel is the *pp* partial wave, conforming to one-photon absorption from each electron as the primary ionization channel. We also see a similarity between the SDI and NSDI radial and energy distributions at the initial stages of the interaction of the field and observe that it is at later stages of the interaction with the field that these asymmetrical radial and energy distributions take their final shape; in practice the SDI mechanism features are mostly developing after the pulse's peak and after the resulting He^+ has had the time to relax to its ground state.

In the NSDI, an oval emission pattern is formed along the equidistant $r_1 = r_2$ diagonal, maximizing the contribution of the electron correlations on their way out (i.e., during the interaction with the laser pulse). This type of radial distribution pattern is found to be generally the case for photon energies less than 54.4 eV.

For the SDI process, the dominant correlation mechanism initially shares some similarity to that of the NSDI regime but soon after the initial interaction with the pulse the absorption of the second photon by the relaxed He^+ introduces an unequal energy sharing; the latter leads to a differentiation of the two-electron radial and energy patterns between the SDI and the NSDI, especially in the *pp* channels. Nevertheless, electron correlation effects continue to be significant for ejection patterns other than the *pp* channel, albeit weaker.

Finally we have calculated the radial ejection patterns as the pulse's central photon energies cross the threshold of 54.4 eV and have observed features that are due to either the sequential or direct DI mechanisms.

In view of the present capabilities of pump-probe experimental schemes in the soft-x-ray wavelength regime it is clear that the present space-time description provides an enhanced view of the process of two-photon DI complementary to the corresponding studies focusing mostly on the final-state energy and momentum joint distributions. It is our intention to work further in this direction by studying more complex atomic systems of experimental interest like neon and argon.

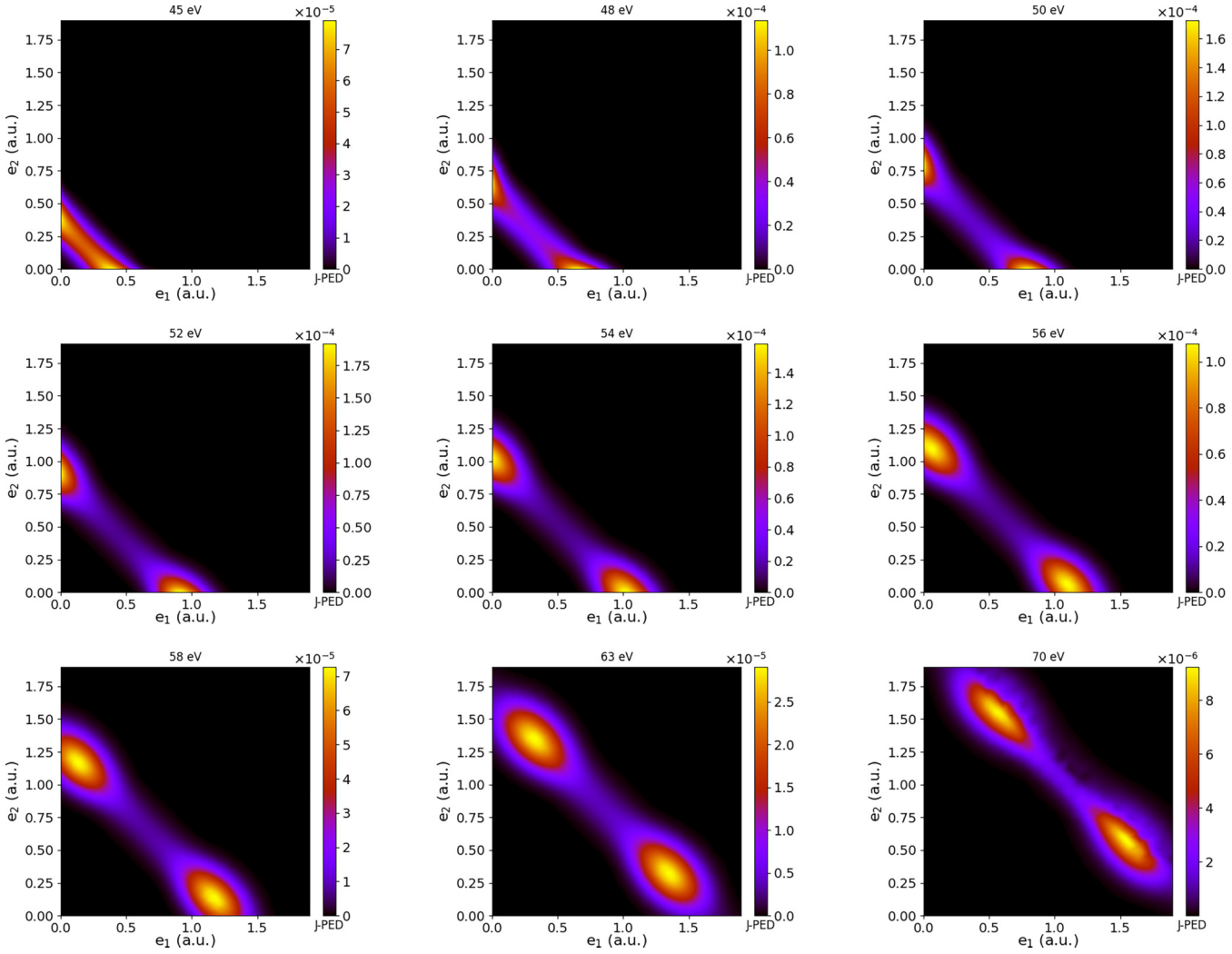

FIG. 10. The (1,1) partial-wave J-PED patterns from the direct to the SDI regime as the average photon energy increases from 45 to 70 eV. Projection time is the end of the pulse (cycle 12). The patterns transition from a mostly shared energy distribution to a doubly peaked distribution. e_1 and e_2 are given in atomic units (a.u.).

ACKNOWLEDGMENTS

A.P. and L.A.A.N. would like to acknowledge the partial support by the Irish Research Council (IRC) via the project ID GOIPG/2017/1257; also A.P. and L.A.A.N. have benefited the most by Andrew Forembski from relevant discussions during the preparation of this paper. The authors would also like to acknowledge partial support from the COST Action CA18222, "Attosecond Chemisty."

[1] N. Berrah, J. Bozek, J. T. Costello, S. Dusterer, L. Fang, J. Feldhaus, H. Fukuzawa, M. Hoener, Y. H. Jiang, P. Johnsson *et al.*, J. Mod. Opt. **57**, 1015 (2010).

[2] I. Grguraš, A. R. Maier, C. Behrens, T. Mazza, T. J. Kelly, P. Radcliffe, S. Düsterer, A. K. Kazansky, N. M. Kabachnik, Th. Tschentscher *et al.*, Nat. Photon. **6**, 852 (2012).

[3] E. Benis, P. Tzallas, L. A. A. Nikolopoulos, M. Kovacev, C. Kalpouzos, D. Charalambidis, and G. D. Tsakiris, New J. Phys. **8**, 92 (2006).

[4] F. Krausz and M. Ivanov, Rev. Mod. Phys. **81**, 163 (2009).

[5] C. Liu and M. Nisoli, Phys. Rev. A **85**, 053423 (2012).

[6] C. Ott, L. Aufleger, T. Ding, M. Rebholz, A. Magunia, M. Hartmann, V. Stooß, D. Wachs, P. Birk, G. D. Borisova *et al.*, Phys. Rev. Lett. **123**, 163201 (2019).

[7] V. Schmidt, *Electron Spectrometry of Atoms Using Synchrotron Radiation* (Cambridge University Press, Cambridge, 1997).

[8] K. C. Kulander, Phys. Rev. A **36**, 2726 (1987).

[9] D. N. Fittinghoff, P. R. Bolton, B. Chang, and K. C. Kulander, Phys. Rev. Lett. **69**, 2642 (1992).

[10] A. F. Starace, in *Corpuscles and Radiation in Matter* (Springer-Verlag, Berlin, 1982), Vol. 1, pp. 1–121.

[11] J. S. Briggs and V. Schmidt, J. Phys. B **33**, R1 (2000).

[12] A. S. Kheifets and I. Bray, J. Phys. B **31**, L447 (1998).
[13] L. Malegat, P. Selles, and A. Kazansky, Phys. Rev. A **60**, 3667 (1999).
[14] D. Dundas, K. T. Taylor, J. S. Parker, and E. S. Smyth, J. Phys. B **32**, L231 (1999).
[15] J. S. Parker, L. R. Moore, D. Dundas, and K. T. Taylor, J. Phys. B **33**, L691 (2000).
[16] P. Tzallas, E. Skantzakis, L. A. A. Nikolopoulos, G. D. Tsakiris, and D. Charalambidis, Nat. Phys. **7**, 781 (2011).
[17] H. Bachau and P. Lambropoulos, Phys. Rev. A **44**, R9(R) (1991).
[18] M. A. Kornberg and P. Lambropoulos, J. Phys. B **32**, L603 (1999).
[19] L. A. A. Nikolopoulos and P. Lambropoulos, J. Phys. B **34**, 545 (2001).
[20] I. F. Barna, J. Wang, and J. Burgdörfer, Phys. Rev. A **73**, 023402 (2006).
[21] E. Foumouo, G. L. Kamta, G. Edah, and B. Piraux, Phys. Rev. A **74**, 063409 (2006).
[22] L. A. A. Nikolopoulos and P. Lambropoulos, J. Phys. B **39**, 883 (2006).
[23] L. A. A. Nikolopoulos and P. Lambropoulos, J. Phys. B **40**, 1347 (2007).
[24] A. S. Kheifets, I. A. Ivanov, and I. Bray, Phys. Rev. A **76**, 025402 (2007).
[25] L. A. A. Nikolopoulos and P. Lambropoulos, New J. Phys. **10**, 025012 (2008).
[26] J. Feist, S. Nagele, R. Pazourek, E. Persson, B. I. Schneider, L. A. Collins, and J. Burgdorfer, Phys. Rev. A **77**, 043420 (2008).
[27] E. Foumouo, P. Antoine, B. Piraux, L. Malegat, H. Bachau, and R. Shakeshaft, J. Phys. B **41**, 051001 (2008).
[28] D. A. Horner, T. N. Rescigno, and C. W. McCurdy, Phys. Rev. A **77**, 030703(R) (2008).
[29] X. Guan, K. Bartschat, and B. I. Schneider, Phys. Rev. A **77**, 043421 (2008).
[30] R. Nepstad, T. Birkeland, and M. Førre, Phys. Rev. A **81**, 063402 (2010).
[31] R. Pazourek, J. Feist, S. Nagele, E. Persson, B. I. Schneider, L. A. Collins, and J. Burgdörfer, Phys. Rev. A **83**, 053418 (2011).
[32] J. Feist, O. Zatsarinny, S. Nagele, R. Pazourek, J. Burgdörfer, X. Guan, K. Bartschat, and B. I. Schneider, Phys. Rev. A **89**, 033417 (2014).
[33] J. Wragg, J. S. Parker, and H. W. van der Hart, Phys. Rev. A **92**, 022504 (2015).
[34] A. A. Sorokin, M. Wellhofer, S. V. Bobashev, K. Tiedtke, and M. Richter, Phys. Rev. A **75**, 051402(R) (2007).
[35] R. Moshammer, Y. H. Jiang, L. Foucar, A. Rudenko, T. Ergler, C. D. Schröter, S. Lüdemann, K. Zrost, D. Fischer, J. Titze *et al.*, Phys. Rev. Lett. **98**, 203001 (2007).
[36] A. Rudenko, L. Foucar, M. Kurka, T. Ergler, K. U. Kühnel, Y. H. Jiang, A. Voitkiv, B. Najjari, A. Kheifets, S. Lüdemann, T. Havermeier, M. Smolarski, S. Schössler, K. Cole, M. Schöffler, R. Dörner, S. Düsterer, W. Li, B. Keitel, R. Treusch, M. Gensch, C. D. Schröter, R. Moshammer, and J. Ullrich, Phys. Rev. Lett. **101**, 073003 (2008).
[37] M. Kurka, A. Rudenko, L. Foucar, K. U. Kühnel, Y. H. Jiang, Th. Ergler, T. Havermeier, M. Smolarski, S. Schössler, K. Cole *et al.*, J. Phys. B **42**, 141002 (2009).
[38] M. Kurka, J. Feist, D. A. Horner, A. Rudenko, Y. H. Jiang, K. U. Kühnel, L. Foucar, T. N. Rescigno, C. McCurdy, R. Pazourek *et al.*, New J. Phys. **12**, 073035 (2010).
[39] P. A. Carpeggiani, E. V. Gryzlova, M. Reduzzi, A. Dubrouil, D. Faccialá, M. Negro, K. Ueda, S. M. Burkov, F. Frassetto, F. Stienkemeie *et al.*, Nat. Phys. **15**, 170 (2019).
[40] E. Foumouo, A. Hamido, P. Antoine, B. Piraux, H. Bachau, and R. Shakeshaft, J. Phys. B **43**, 091001 (2010).
[41] P. Lambropoulos, L. A. A. Nikolopoulos, and M. G. Makris, Phys. Rev. A **72**, 013410 (2005).
[42] L. A. A. Nikolopoulos, Phys. Rev. Lett. **111**, 093001 (2013).
[43] P. K. Maroju, C. Grazioli, M. D. Fraia, M. Moioli, D. Ertel, H. Ahmadi, O. Plekan, P. Finetti, E. Allaria, L. Giannessi *et al.*, Nature (London) **578**, 386 (2020).
[44] I. Makos, I. Orfanos, E. Skantzakis, I. Liontos, P. Tzallas, A. Forembski, L. A. A. Nikolopoulos, and D. Charalambidis, High Power Laser Sci. Eng. **8**, e44 (2020).
[45] Z. X. Zhao and C. D. Lin, Phys. Rev. A **71**, 060702(R) (2005).
[46] Z. Q. Yang, D. F. Ye, T. Ding, T. Pfeifer, and L. B. Fu, Phys. Rev. A **91**, 013414 (2015).
[47] L. Medišauskas, R. Y. Bello, A. Palacios, A. González-Castrillo, F. Morales, L. P. mak, O. Smirnova, F. Martín, and M. Y. Ivanov, J. Phys. B **50**, 144001 (2017).
[48] M. Straub, T. Ding, M. Rebholz, G. D. Borisova, A. Magunia, H. Lindenblatt, S. Meister, F. Trost, Y. Wang, S. Palutke, M. Braune, S. Düsterer, R. Treusch, C. H. Greene, R. Moshammer, T. Pfeifer, and C. Ott, Phys. Rev. Lett. **129**, 183204 (2022).
[49] L. A. A. Nikolopoulos, Comput. Phys. Commun. **150**, 140 (2003).
[50] A. Forembski and L. A. A. Nikolopoulos, Comput. Phys. Commun. **291**, 108820 (2023).
[51] L. A. A. Nikolopoulos and H. Bachau, Phys. Rev. A **94**, 053409 (2016).
[52] H. Bachau and L. A. A. Nikolopoulos, J. Phys. Chem A **122**, 1574 (2018).
[53] F. Martín, J. Phys. B **32**, R197 (1999).
[54] H. Bachau, E. Cormier, P. Decleva, J. E. Hansen, and F. Martín, Rep. Prog. Phys. **64**, 1815 (2001).
[55] L. A. A. Nikolopoulos, Phys. Rev. A **73**, 043408 (2006).
[56] A. Palacios, C. W. McCurdy, and T. N. Rescigno, Phys. Rev. A **76**, 043420 (2007).
[57] B. Piraux, J. Bauer, S. Laulan, and H. Bachau, Eur. Phys. J. D. **26**, 7 (2003).
[58] C. Ó Broin and L. A. A. Nikolopoulos, Comput. Phys. Commun. **185**, 1791 (2014).
[59] J. Tulkki, G. Armen, T. Aberg, B. Crasemann, and M. Chen, Z. Phys. D **5**, 241 (1987).
[60] H. Bachau, Phys. Rev. A **83**, 033403 (2011).